Angewandte Chemie International Edition

Angewandte International Edition Chemie

How to cite: *Angew. Chem. Int. Ed.* **2026**, e4295699
doi.org/10.1002/anie.4295699

RESEARCH ARTICLE

Cyclic $P_3O_9^{3-}$ Trimer: A Network Former for Amorphous Superionic Conductors in Sodium Solid-State Batteries

Siyuan Zhang[1,2] | Jiacong Li[3,4] | Yuge Cao[3,4] | Yifeng Zhao[3,4] | Zhongxing Xu[1] | Zhuoran Lv[1] | Long Yang[5] | Chaohong Guan[6] | Zhangliu Tian[3,4] | Wujie Dong[1,2] | Haijie Chen[7] | Fuqiang Huang[1,2]

[1]Key Laboratory of Intelligent Creation For Extreme Energy Materials of Ministry of Education, School of Materials Science and Engineering and Zhang jiang Institute for Advanced Study, Shanghai Jiao Tong University, Shanghai, China | [2]Inner Mongolia Research Institute, Shanghai Jiao Tong University, Hohhot, China | [3]Shanghai Institute of Ceramics, Chinese Academy of Sciences, Shanghai, China | [4]Center of Materials Science and Optoelectronics Engineering, University of Chinese Academy of Sciences, Beijing, China | [5]School of Materials Science and Engineering, Tongji University, Shanghai, China | [6]National Engineering Research Center of Light Alloy Net Forming, School of Materials Science and Engineering, Shanghai Jiao Tong University, Shanghai, China | [7]State Key Laboratory of Advanced Fiber Materials, Institute of Functional Materials, College of Materials Science and Engineering, Donghua University, Shanghai, P.R. China

Correspondence: Wujie Dong (dongwujie@sjtu.edu.cn) | Haijie Chen (haijie.chen@dhu.edu.cn) | Fuqiang Huang (huangfq@sjtu.edu.cn)

Received: 31 December 2025 | **Revised:** 3 June 2026 | **Accepted:** 4 June 2026

Keywords: all-solid-state sodium-ion batteries | amorphous oxyhalide | cyclic trimetaphosphate | interfacial compatibility | solid-state electrolytes

ABSTRACT

Achieving solid-state electrolytes (SSEs) that combine fast Na^+ conduction, high-voltage stability, and deformability remains a formidable challenge for all-solid-state sodium-ion batteries (ASSNIBs). Here, we introduce a cyclic trimetaphosphate anion ($P_3O_9^{3-}$) as a transformative network-forming unit to construct a new family of amorphous oxyhalide SSEs via facile mechanochemical synthesis. The unique nine-oxygen-donor architecture of $P_3O_9^{3-}$ enables robust, three-dimensional coordination with metal chlorides (MCl_n, M = Zr, Ta, Hf, Nb, Al), forming a rigid yet disordered framework where isolated Cl^- anions are strategically liberated. This distinctive structure enables a dynamic anion-assisted transport mechanism: the $P_3O_9^{3-}$-bridged network provides stable conduction channels, while the mobile Cl^- anions dynamically assist Na^+ hopping by mitigating steric and electrostatic barriers, collectively achieving an ultralow activation energy of 0.33 eV. The optimized electrolyte exhibits a high room-temperature ionic conductivity of 0.80 mS·cm^{-1} and a wide electrochemical window of 1.4–4.2 V. ASSNIBs assembled with a $NaNi_{0.33}Fe_{0.33}Mn_{0.33}O_2$ cathode demonstrate stable cycling at 4.2 V, retaining 92% capacity after 300 cycles at 0.5C. This work pioneers the use of macrocyclic polyphosphates in SSEs, establishing a new design paradigm that simultaneously addresses ionic conductivity, stability, and interfacial compatibility.

1 | Introduction

The global transition toward renewable energy has spurred urgent demand for safer, low-cost, and high-performance large-scale energy storage systems [1–3]. All-solid-state sodium-ion batteries (ASSNIBs) stand out as a compelling candidate, leveraging sodium's natural abundance and low cost while eliminating the safety hazards of flammable liquid electrolytes [4]. However, the practical deployment of ASSNIBs is bottlenecked by solid-state electrolytes (SSEs) that struggle to reconcile three core requirements: fast Na^+ conductivity, wide electrochemical stability window (compatible with high-voltage cathodes > 4.0 V),

Siyuan Zhang, Jiacong Li, and Yuge Cao contributed equally to this work.

and robust interfacial compatibility/mechanical ductility [5]. This "trilemma" stems from the inherent trade-offs of existing SSE designs: oxide-based SSEs offer stability but suffer from rigid lattices and poor ion transport [6, 7]; sulfide SSEs exhibit high conductivity yet are air-sensitive and limited by narrow voltage windows [8, 9]; while conventional halide SSEs, despite favorable oxidative stability, lack structural flexibility and rely on static lattices that hinder dynamic ion migration [10, 11]. Thus, developing new SSEs that overcome these limitations remains essential for advancing ASSNIBs.

To address this challenge, researchers have explored oxyhalide hybrid systems that merge the stability of oxides with the ion mobility of halides [12, 13], alongside amorphous structures that eliminate grain boundary resistance and enhance mechanical compliance [14–16]. Recent advances have been further catalyzed by the emergence of non/low-crystalline halide superionic conductors [17] and, more recently, by the strategic design of heterogeneous structures that integrate high-coordination and low-coordination frameworks to achieve synergistic Na^+ transport across crystalline, amorphous, and interfacial regions [18]. A key design strategy involves integrating anion groups as network formers to bridge high-valent transition metal cations, constructing rigid frameworks for ion conduction [19]. For instance, recent work by Sun's group [13] demonstrated the use of carbonate groups (CO_3^{2-})—with only three coordination sites—to modulate halide structures, reducing costs while improving structural integrity. However, these small polyatomic anions offer limited coordination versatility, failing to form extensive, three-dimensional networks; monatomic anions (O^{2-}, N^{3-}) are even more constrained, leading to static frameworks that create unavoidable steric hindrance for Na^+ migration [20, 21]. Moreover, the synthesis of such systems often requires harsh conditions, as the formation of stable cation-anion bonds (*e.g.*, M-O) lacks sufficient thermodynamic driving force [22, 23].

Herein, we break from conventional anion design by pioneering the use of cyclic trimetaphosphate ($P_3O_9^{3-}$) trimers as a supreme network-forming unit—an unprecedented choice for SSEs. This design offers dual transformative advantages rooted in its structure and thermodynamics. Structurally, $P_3O_9^{3-}$ features three phosphorus atoms linked by intramolecular P-O-P bridges (forming three skeleton oxygen atoms), surrounded by six peripheral oxygen atoms (total nine oxygen donors). Unlike carbonate's three limited sites, these six peripheral oxygen atoms are all accessible for multidentate coordination with high-valent metal cations of M^{4+}/M^{5+}, (M = Zr, Ta, Hf), enabling binding in three-dimensional directions to construct an extensive, divergent amorphous network—far more robust and interconnected than networks formed by single/anion groups. Thermodynamically, as a sodium salt ($Na_3P_3O_9$), it exhibits a strong tendency to form Na—Cl bonds when reacted with metal chlorides (MCl_n), which is far more favorable than Na—O bond formation. This inherent stability driving force means that mild high-energy ball milling is sufficient to break the original bonds and induce structural reconstruction, facilitating facile synthesis of the target oxyhalide SSEs. The distinctive configuration leads to a cooperative transport paradigm, in which a rigid continuous network provides stable migration channels while dynamically mobile anions mediate low-energy Na^+ hopping, collectively surpassing the constraints of static crystalline frameworks. The $P_3O_9^{3-}$—bridged 3D network acts as a stable "rail," providing continuous, unobstructed channels for Na^+ migration with a robust framework. Meanwhile, the integration of MCl_n generates isolated Cl^- anions within the network—functioning as "dynamic wheels" with low effective mass. These Cl^- ions dynamically adjust positions in response to Na^+ migration: electrostatically attracting Na^+ to reduce Coulombic barriers while vacating sites to mitigate steric hindrance. This synergistic interaction slashes the Na^+ diffusion barrier, enabling fast ion transport with a low activation energy.

Guided by this principle, we synthesized a series of amorphous oxyhalide SSEs via mechanochemical reactions between $Na_3P_3O_9$ and metal chlorides (MCl_n). The optimized SSE delivers a room-temperature Na^+ conductivity of 0.80 mS·cm^{-1}, an ultrawide electrochemical window (1.4–4.2 V), and excellent mechanical ductility (Young's modulus ~0.15 GPa). When paired with the $NaNi_{0.33}Fe_{0.33}Mn_{0.33}O_2$ high-voltage cathode, the ASSNIB operates stably at 4.2 V, retaining 92% capacity after 300 cycles at 0.5C. This study not only pioneers cyclic trimetaphosphate trimers for SSE design but also establishes a new paradigm of "3D coordination network + thermodynamic driving force + dynamic ion transport"—offering a generalizable strategy to overcome the SSE trilemma and advance practical ASSNIBs.

2 | Results and Discussion

2.1 | Synthesis and Characterization of Amorphous SSEs

A series of $xNa_3P_3O_9$-MCl_n (M = Zr, Ta, Hf, Nb, and Al) SSEs were synthesized through a high-energy ball milling process of $Na_3P_3O_9$ and MCl_n in an argon atmosphere. Here x is the molar ratio of the precursor shown in Equation (1). Considering both ionic conductivity and material cost, the $ZrCl_4$-based system (denoted NZPOC) was chosen as the focus for subsequent detailed study.

$$xNa_3P_3O_9 + MCl_n \rightarrow Na_{3x}\left[MCl_{n-3x}(P_3O_9)_x\right]Cl_{3x} \quad (1)$$

The $P_3O_9^{3-}$ anion contains three P atoms bridged by P—O—P bonds (three skeletal O) and six peripheral O atoms (Figure 1a). Each peripheral O can engage in multidentate coordination with M^{n+} cations (M = Zr, Ta, Hf, Nb, Al). This provides three-dimensional binding sites that direct the assembly of a widely branched, robust amorphous network. The resulting structure is substantially more interconnected than networks formed by monodentate or small anion units. This enables the construction of the three-dimensional amorphous network shown in Figure 1b, where $P_3O_9^{3-}$ rings bridge metal-halide units. In this structure, the $P_3O_9^{3-}$-linked framework serves as a stable "rigid rail," providing continuous and open migration channels. Concurrently, the incorporated Cl^- ions act as "mobile wheels," dynamically repositioning to electrostatically guide and accommodate Na^+, which collectively lowers the diffusion barrier and underpins the high ionic conductivity. This structural arrangement is directly visualized in the molecular dynamics snapshot (Figure 1c) and further illustrated in Figure S1, which shows the coordination polyhedra of Zr and Na together with the $P_3O_9^{3-}$ rings. The phase composition of the synthesized materials

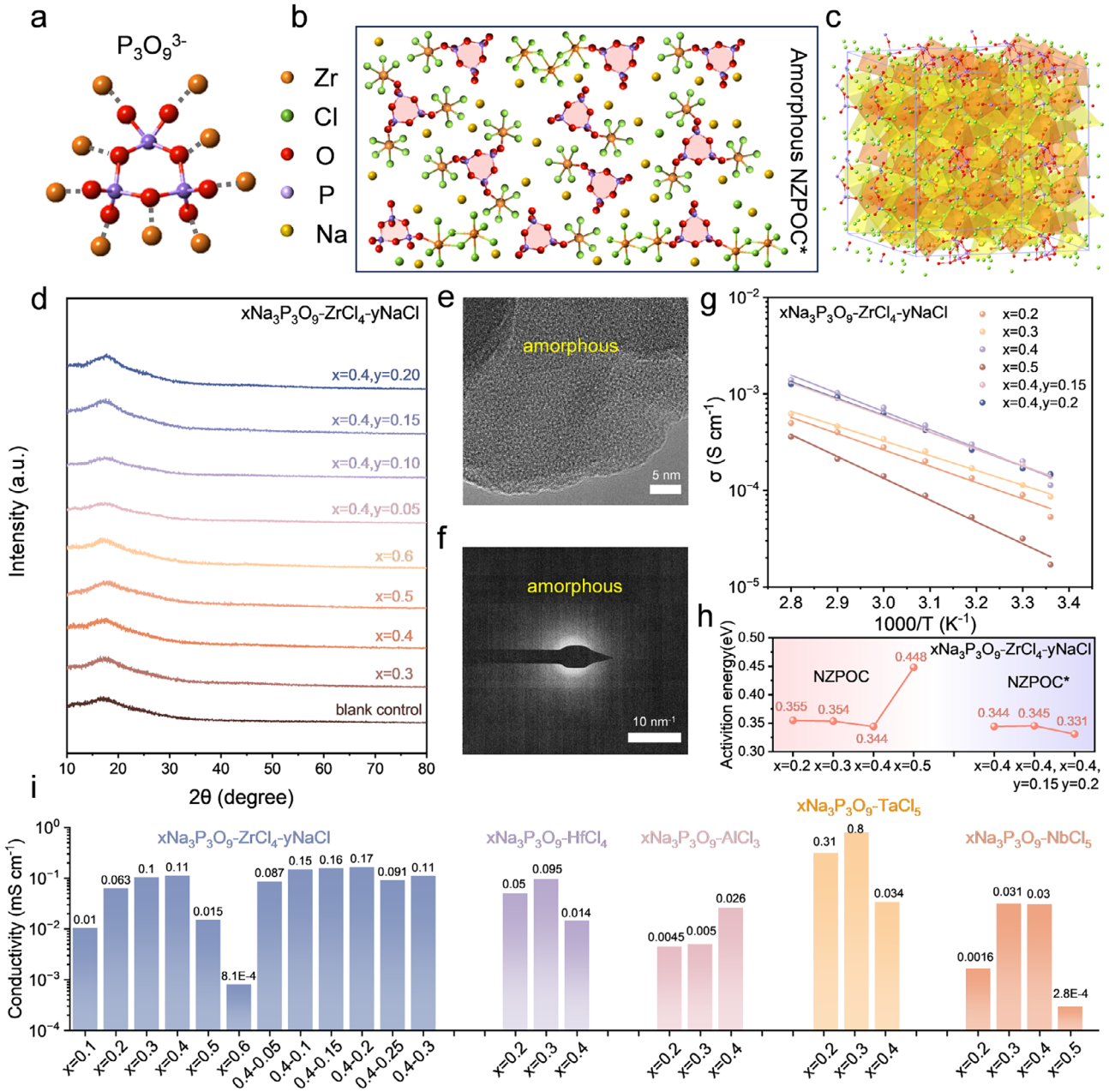

FIGURE 1 | (a) The coordination environment of $P_3O_9^{3-}$. (b) The structural schematic of amorphous NZPOC* SSE. (c) Molecular dynamics (MD) simulations of the NZPOC* electrolyte showing the coordination polyhedra of Zr (orange) and Na (yellow), together with the $P_3O_9^{3-}$ rings (red and purple). (d) XRD patterns for the $x$$Na_3P_3O_9$-$ZrCl_4$-$y$NaCl ($0.3 \leq x \leq 0.6$, $0.05 \leq y \leq 0.20$) SSEs. (e, f) HRTEM images of the NZPOC* SSE. (g) The temperature (T) dependent ionic conductivities (σ) of the as-prepared $x$$Na_3P_3O_9$-$ZrCl_4$-$y$NaCl SSEs. (h) The corresponding activation energy (E) for $x$$Na_3P_3O_9$-$ZrCl_4$-$y$NaCl SSEs. (i) Comparison of the ionic conductivity at 25°C for the amorphous $x$$Na_3P_3O_9$-$MCl_n$ (M = Zr, Hf, Al, Ta, and Nb) SSEs.

was examined by powder X-ray diffraction (XRD). As shown in Figure 1d, all NZPOC compositions (with $Na_3P_3O_9$ fractions $0.1 \leq x \leq 0.6$) exhibit featureless diffraction patterns, confirming their fully amorphous structure. This amorphous nature was consistent across all other oxyhalide electrolytes prepared in this study (Figure S2). The XRD patterns of all samples exhibit no distinct diffraction peaks, which indicates the completely amorphous nature of the materials. The broad hump at approximately 18° can be attributed to the high-temperature tape used during the measurement. Further structural confirmation was provided by high-resolution transmission electron microscopy (HRTEM). The images reveal a featureless morphology devoid of lattice fringes, while the corresponding diffuse halo in the amorphous regions corroborates the absence of long-range crystallinity (Figure S3).

The room-temperature ionic conductivity of the NZPOC electrolytes, measured by electrochemical impedance spectroscopy (EIS, Figures S4 and S5), exhibited a nonmonotonic dependence on the $Na_3P_3O_9/ZrCl_4$ molar ratio, initially rising and then decreasing with increasing $Na_3P_3O_9$ content. A maximum conductivity of 0.11 mS cm^{-1} was achieved for the composition with $x = 0.4$. This trend was consistently observed across other oxyhalide systems, which demonstrated appreciable to high ionic conductivities, as evidenced by their respective EIS spectra (Figures S6

and S7). Among these, the optimized $0.3Na_3P_3O_9$-$TaCl_5$ (NTPOC) composition achieves a notable room-temperature conductivity of 0.80 mS cm^{-1} (Figure 1i). In addition to the amorphous electrolytes synthesized using different metal chlorides, we also successfully prepared Na_3PO_4-$ZrCl_4$, $Na_4P_2O_7$-$ZrCl_4$, and $Na_5P_3O_{10}$-$ZrCl_4$ solid electrolytes. These materials exhibit an amorphous structure and show appreciable ionic conductivity (Figures S8–S12).

To further enhance ionic conductivity, a small amount of NaCl was introduced as an additive during the mechanochemical synthesis, resulting in a modified series denoted as $x$$Na_3P_3O_9$-$ZrCl_4$-$y$NaCl (denoted as NZPOC*). As shown in Figures S13 and S14, the ionic conductivity of NZPOC* first increased and then decreased with increasing NaCl content (y). Notably, a conductivity of 0.17 mS cm^{-1} was achieved under the optimal conditions of $y = 0.2$, significantly higher than that of Na_2ZrCl_6 (Figure S15). This value is superior to those of most known zirconium-based amorphous solid electrolytes [24, 25]. The amorphous structure of the NaCl-modified compositions was confirmed by XRD (Figure S16) and HRTEM (Figures 1e,f). The absence of distinct diffraction peaks in the XRD patterns, together with the featureless morphology lacking lattice fringes and the corresponding diffuse halo in the HRTEM images, collectively confirms the completely amorphous nature of the NZPOC*.

The temperature dependence of ionic conductivity and the corresponding activation energies for the NZPOC and NZPOC* series are presented in Figure 1g,h, respectively. As the $Na_3P_3O_9$ content (x) increases, the activation energy passes through a minimum, exhibiting an inverse correlation with the room-temperature conductivity. Among all compositions, $0.4Na_3P_3O_9$-$ZrCl_4$-0.2NaCl SSE demonstrated the highest conductivity (0.17 mS cm^{-1}) and the lowest activation energy (0.33 eV). These results suggest that the designed amorphous, solvent-like network facilitates efficient ion transport both in the bulk and across interfaces—a point that will be structurally elucidated in later sections. Additionally, NZPOC* exhibits electronic insulation (Figure S18) alongside its fast Na^+ conduction. This characteristic is crucial for suppressing current leakage and ensuring long-term cycling stability in ASSNIBs.

The practical stability of NZPOC* was evaluated by monitoring its ionic conductivity under ambient air exposure (relative humidity ≈ 5%, 25°C) over 12 h (Figure S19a and Table S1). After 12 h of exposure, the conductivity decreased from 0.17 mS cm^{-1} to 0.02 mS cm^{-1}, while the cold-pressed pellets exhibited no visible color change or macroscopic degradation throughout the exposure period (Figure S20a). For comparison, the control sample $0.4Na_3PO_4$-$ZrCl_4$ showed a more severe conductivity drop to 0.01 mS cm^{-1} after 12 h, accompanied by visible graying of the pellet (Figures S19b and S20b). These results indicate that NZPOC* requires inert handling but is sufficiently stable for use in protected environments.

3 | Local Structure Exploration of NZPOC* Amorphous SSEs

The local chemical environment and overall structure of the NZPOC* SSEs were elucidated using a suite of spectroscopic techniques. The results reveal a homogeneous, fully amorphous structure arising from the coupling between discrete cyclic molecules and extended chloride chains.

Figure 2a displays the X-ray photoelectron spectroscopy (XPS) spectrum of the Zr 3d region for the $x$$Na_3P_3O_9$-$ZrCl_4$-0.2NaCl SSEs. Two prominent peaks at 182.9 and 185.4 eV are assigned to the Zr $3d_{5/2}$ and Zr $3d_{3/2}$ orbitals, respectively, characteristic of Zr—Cl bonds [26]. Concurrently, an additional doublet appears at 183.8 and 186.2 eV, confirming the formation of Zr—O bonds. With increasing $Na_3P_3O_9$ content (x), the Zr $3d_{5/2}$ peak shifts to higher binding energy, indicating a gradual increase in the oxidation state of Zr. This shift results from the greater number of Zr—O bonds formed upon incorporation of cyclic phosphate, wherein the higher electronegativity of oxygen withdraws electron density from Zr toward the anionic framework. The O 1s XPS spectrum corroborates the presence of bridging oxygen [27, 28], which links the $P_3O_9^{3-}$ groups to Zr centers, alongside nonbridging oxygen species (Figure S24).

Additionally, the Cl 2p XPS spectra (Figure 2b) exhibit spin-orbit doublets (Cl $2p_{3/2}$ and Cl $2p_{1/2}$) at binding energies of 198.5 and 200.2 eV, respectively [29]. An x rises, the Cl $2p_{3/2}$ peak also shifts to higher binding energy, reflecting an elevated oxidation state of Cl. This trend is attributed to enhanced Zr—O bonding, which renders Zr more electropositive and consequently withdraws electron density from the bonded Cl atoms. Meanwhile, the P 2p XPS spectrum (Figure 2c) shows two peaks at binding energies of 134.8 and 135.3 eV, which are assigned to the P $2p_{3/2}$ and P $2p_{1/2}$ states, respectively. The strengthening of Zr—O bonds with higher x modifies the local electronic environment of phosphorus. This leads to a weakening of the P—O bonding character, which increases the electron density on phosphorus. As a result, the P $2p_{3/2}$ peak shifts to a lower binding energy, corresponding to a reduced oxidation state. Collectively, these systematic shifts in binding energy highlight a key structural feature of the NZPOC* electrolyte: the chemical integration of discrete cyclic phosphate units with one-dimensional inorganic halide chains within its amorphous network.

Zr K-edge extended X-ray absorption fine structure (EXAFS) spectroscopy was employed to probe the atomic-scale chemical environment of the amorphous NZPOC and NZPOC* SSEs. As shown in Figure 2g, the Zr K-edge X-ray absorption near-edge structure (XANES) spectra of NZPOC and NZPOC* exhibit features similar to those of crystalline $ZrCl_4$. The absorption-edge energy (E_0) of NZPOC and NZPOC* lies between those of ZrO_2 and $ZrCl_4$, consistent with partial oxidation of Zr upon reaction with $Na_3P_3O_9$. In the white-line region, crystalline $ZrCl_4$ displays a distinct splitting, corresponding to its three discrete Zr—Cl bond lengths. In contrast, the NZPOC and NZPOC* spectra present a smooth, merged profile, indicating a more uniform distribution of Zr—(Cl/O) bond lengths in the amorphous matrix. This suggests that the nearest-neighbor distances around Zr are more homogeneous in NZPOC and NZPOC* than in its crystalline precursor. The Zr K-edge EXAFS data in k-space (Figure S25) further reveal a low-k phase shift, a spectroscopic signature that Zr—O bonding induces local disorder and elongation of the Zr—Cl bonds [30, 31]. These structural insights align well with the XPS results discussed earlier, collectively confirming the hybrid Zr—Cl/O coordination environment in the amorphous electrolyte.

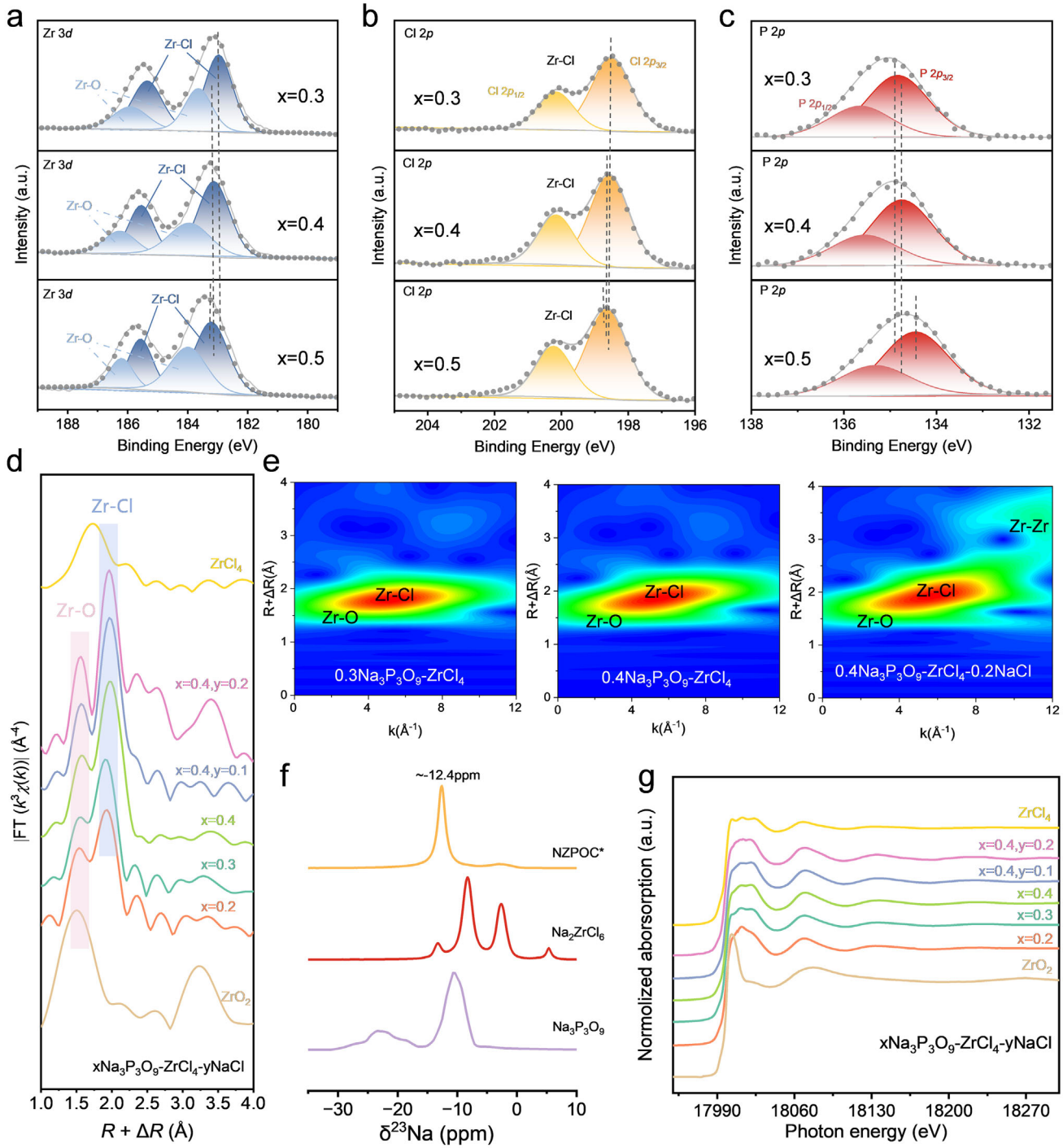

FIGURE 2 | (a–c) Zr 3*d* XPS (a), Cl 2*p* XPS (b), and P 2*p* XPS (c). (d) Fourier-transform (FT) EXAFS spectra of the xNa$_3$P$_3$O$_9$-ZrCl$_4$-yNaCl SSEs at the Zr *K*-edge, respectively. ZrCl$_4$ and ZrO$_2$ are reference samples. (e) Wavelet-transformed (WT) EXAFS spectrum of 0.3Na$_3$P$_3$O$_9$-ZrCl$_4$, 0.4Na$_3$P$_3$O$_9$-ZrCl$_4$, and 0.4Na$_3$P$_3$O$_9$-ZrCl$_4$-0.2NaCl SSEs at the Zr *K*-edge. A k^3 weighting was used. (f) ^{23}Na NMR spectra of NZPOC*, Na$_2$ZrCl$_6$ and Na$_3$P$_3$O$_9$. (g) Zr *K*-edge XANES spectra of ZrCl$_4$, ZrO$_2$, and the xNa$_3$P$_3$O$_9$-ZrCl$_4$-yNaCl SSEs.

To elucidate the local coordination environment of Zr cations, Zr *K*-edge Fourier transform (FT) and wavelet transform (WT) analyses were performed on the NZPOC and NZPOC* electrolytes (Figure 2d,e). The FT-EXAFS spectra reveal coordination peaks corresponding to Zr—O (~1.9 Å) and Zr—Cl (~2.4 Å) bonds [31]. With increasing Na$_3$P$_3$O$_9$ content, the intensity of the Zr—O peak grows, indicating stronger Zr—O interaction, while the Zr—Cl bond length elongates relative to that in pristine ZrCl$_4$. Using crystalline ZrO$_2$ and ZrCl$_4$ as references for characteristic scattering paths (Figure S26), phase-uncorrected WT-EXAFS further identifies O, Cl, and Zr as the nearest neighbors around Zr in NZPOC and NZPOC* (Figures 2e and S27) [30, 32]. Quantitative EXAFS fitting reveals the average local coordination environment around Zr in NZPOC*, with coordination numbers of approximately 2.0 for oxygen and 4.0 for chlorine (Figure S28 and Table S2). Further supporting evidence from pair distribution

function (PDF) analysis confirms that oxygen and chlorine atoms constitute the nearest coordination shell of zirconium. As shown in Figure S29, the PDF profile exhibits two distinct peaks at approximately 1.9 and 2.4 Å, corresponding to Zr—O and Zr—Cl correlations, respectively. These distances are in excellent agreement with the bond lengths derived from EXAFS fitting, confirming the mixed oxygen–chlorine coordination environment around Zr centers. Moreover, a notable peak at ~3.5 Å is observed, which is assigned to Zr–Zr correlations. This feature indicates the presence of Zr-centered polyhedral dimers or edge-sharing connectivity within the amorphous network, consistent with the EXAFS analysis. The absence of sharp peaks beyond 5 Å in the PDF pattern further confirms the fully amorphous nature of the material, with no detectable crystalline impurities—in line with the featureless XRD patterns and HRTEM observations. Together with the XPS results, these findings confirm the effective structural integration of cyclic phosphate units with chloride-based chains in the amorphous network.

^{23}Na solid-state nuclear magnetic resonance (ssNMR) spectroscopy was employed to characterize the local sodium environment and structural integration within the amorphous NZPOC* matrix (Figure 2f). The spectrum of NZPOC* exhibits a resonance at –12.4 ppm, distinct from that of crystalline Na_2ZrCl_6, confirming the absence of this phase. Compared with the signal of crystalline $Na_3P_3O_9$, this peak shows an upfield shift of the negative chemical shift, indicating that Na^+ ions preferentially coordinate with Cl^- and migrate primarily along chloride-rich pathways [33, 34]. Such an ionic transport mechanism contributes to the enhanced overall conductivity of the electrolyte. Furthermore, no peak is observed at 7.2 ppm, which is characteristic of crystalline NaCl, confirming that no segregated NaCl phase is present [35].

Time-of-flight secondary ion mass spectrometry (TOF-SIMS) was employed to identify the zirconium-containing oxyhalide polyanions within the amorphous NZPOC* electrolyte. As shown in Figures 3a and S30, a series of anionic clusters with the general formula $[Zr_aO_bP_cCl_d]^{(2b+5c+d-4a)-}$ were detected. The mass spectra revealed a variety of anionic species. Mononuclear anions such as $[ZrO_2Cl_2]^-$, $[ZrOCl_3]^-$, and $[ZrClP_2O_7]^-$ were identified, alongside polynuclear clusters conforming to the $[Zr_aO_bP_cCl_d]^{(2b+5c+d-4a)-}$ series. These clusters range from the dimer $[Zr_2O_3Cl_3]^-$ and the trimer $[Zr_3P_3O_9Cl_{13}]^{4-}$ to isolated $[P_3O_9]^{3-}$ groups. The TOF-SIMS data for the additional polyanionic clusters are presented in Figure S30, with the corresponding representative structures shown in Figure S31. Each anionic species, such as $[Zr_2O_3Cl_3]^-$, can exist in multiple configurations, as illustrated in Figure S32. It should be noted that TOF-SIMS signal intensities are influenced by matrix effects, ionization efficiency, and fragmentation behavior, and therefore do not directly represent quantitative abundances. Additionally, isotopic distributions give rise to satellite peaks adjacent to the main spectral features.

Based on the foregoing analysis, a coherent structural picture of the NZPOC* amorphous electrolyte emerges. The cyclic $P_3O_9^{3-}$ units function as multidentate bridging ligands, coordinating to zirconium chloride octahedra to form an extended, disordered network characterized by halogen-oxygen mixed coordination. Within this network, the $P_3O_9^{3-}$-bridged framework serves as a rigid, continuous scaffold that provides structural integrity and defines open migration channels. Crucially, a population of Cl^- anions remains only weakly bound to the network (as evidenced by EXAFS and XPS), granting them local mobility. Quantitative support for this differential mobility comes from molecular dynamics simulations: the mean square displacement (MSD) of Zr is significantly larger than that of P, confirming that the Zr-centered chlorido-zirconate chains are dynamically flexible [36], whereas the $P_3O_9^{3-}$ rings remain relatively rigid (Figure S33). These "dynamic wheels" can transiently reposition in response to migrating Na^+: they electrostatically attract approaching Na^+ to reduce Coulombic barriers while vacating sites to mitigate steric hindrance. This synergy, in which the rigid network ensures stable conduction pathways and mobile Cl^- anions dynamically facilitate Na^+ hopping, collectively underpins the low activation energy (0.33 eV) and high ionic conductivity observed.

4 | Electrochemical Performance of ASSNIBs With NZPOC* SSEs

The compatibility of NZPOC* SSEs with electrodes was assessed to evaluate their feasibility for ASSNIBs. The ASSNIB cell consisted of Na_2Sn anode and $NaNi_{0.33}Fe_{0.33}Mn_{0.33}O_2$ (NNFMO) cathode, separated by a bilayer electrolyte comprising NZPOC* and Na_3PS_4 (NPS). This NZPOC*-NPS bilayer design was employed to mitigate interfacial reactions between the NZPOC electrolyte and the Na_2Sn anode (Figure 4a). The ASSNIB was fabricated by cold-pressing. SEM imaging combined with EDS mapping (Figures S34–S37) confirmed intimate contact at both the cathode | NZPOC* and NZPOC* | NPS interfaces, which facilitates efficient Na^+ transport across the cell.

Linear sweep voltammetry (LSV) was employed to examine the electrochemical stability of NZPOC* (Figure S38). The measured window spans from 1.4 to 4.2 V relative to Na^+ / Na_2Sn, indicating favorable stability for use with high-voltage cathode materials. The NZPOC*-based ASSNIB employing the NZPOC* SSE demonstrates exceptional electrochemical performance. It delivers a high initial discharge capacity of 138.6 mAh g^{-1} at 0.1C (1C = 120 mAh g^{-1}) with a remarkably high initial coulombic efficiency of 92.2%, within a voltage window of 2.0–4.1 V (Figure 4b,c). Excellent rate capability is demonstrated, with capacities of 138.6, 122.6, 108.9, 90.3, and 39.2 mAh g^{-1} at rates of 0.1C, 0.2C, 0.3C, 0.5C, and 1C, respectively. Furthermore, the cell exhibits impressive long-term cyclability, retaining 80% of its capacity after 207 cycles at 0.5C (Figures 4b and S40). When operated under an extended voltage window of 2.8-4.2 V, the cell achieves an even higher initial discharge capacity of 147.4 mAh g^{-1} with an initial Coulombic efficiency of 93.5% (Figure 4e,f). Its rate performance remains outstanding, delivering reversible capacities of 147.4, 126.2, 107.4, 75.7, and 48.2 mAh g^{-1} at current rates of 0.1C, 0.2C, 0.3C, 0.5C, and 1C, respectively. Remarkably, the battery maintains 92% of its capacity after 300 cycles at 0.5C, showcasing exceptional cycling stability (Figure 4g,h). The well-maintained charge–discharge profiles throughout extended cycling further confirm excellent electrochemical reversibility and interfacial stability.

Additionally, full cells were also assembled and tested using SSEs synthesized from $Na_3P_3O_9$ with various halides. Following the

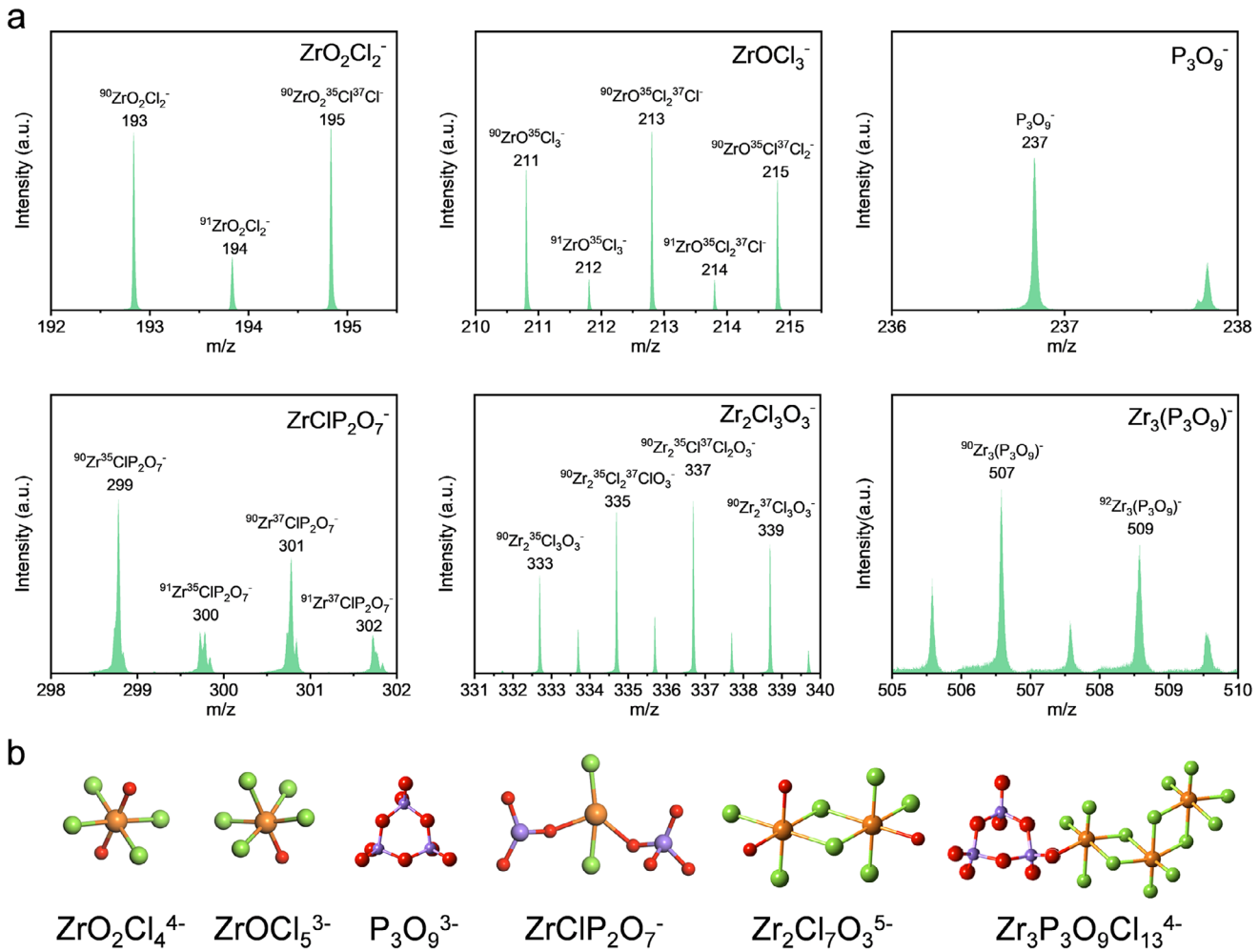

FIGURE 3 | (a) Negative-ion TOF-SIMS of NZPOC* pellet. (b) Optimized geometries of possible Zr-centered oxyhalide polyanions (orange: Zr, green: Cl, red: O, purple: P).

same cell assembly protocol, ASSNIB cells based on $Na_3P_3O_9$-$TaCl_5$(NTPOC) SSEs were constructed with an NNFMO cathode and a Na_2Sn anode. The cell delivers an initial discharge capacity of 160.7 mAh g^{-1} with an initial coulombic efficiency of 96.1%. It demonstrates notable rate capability, with reversible capacities of 160.7, 143.7, 128.6, 115.3, and 79.6 mAh g^{-1} at 0.1C, 0.2C, 0.3C, 0.5C, and 1C, respectively (Figure S44). Moreover, the cell shows stable long-term cycling performance, retaining 82% of its capacity after 160 cycles at 0.5C. they demonstrated stable cycling performance, showing practical potentials of the SSE family.

In summary, the NZPOC* SSEs enable high-performance ASSNIBs paired with high-voltage NNFMO cathodes. These cells exhibit high initial discharge capacity, excellent rate capability, and outstanding long-term cycling stability. The consistently high Coulombic efficiency and stable charge–discharge profiles confirm excellent interfacial compatibility and electrochemical reversibility.

5 | Interfacial Compatibility

Interfacial compatibility is a critical determinant of long-term cycling stability in ASSNIBs. Atomic force microscopy (AFM) measurements reveal a low Young's modulus of ~0.15 GPa for NZPOC* (Figure 5a–d), indicating its mechanically soft and compliant nature. This inherent softness enables conformal contact with cathode particles during electrode fabrication and accommodates interfacial strain during cycling—both essential for durable battery operation. Correspondingly, scanning electron microscopy (SEM) combined with energy dispersive spectroscopy (EDS) demonstrates that NNFMO cathode particles are fully embedded and uniformly wrapped by the NZPOC* electrolyte (Figures S34–S37). The intimate interfacial contact, resulting from the high deformability and adhesion of NZPOC* during cold-pressing, is further visualized at the cathode-layer interface (Figure 5e) and at its junction with the NPS interlayer (Figure 5f). Collectively, these favorable interfacial characteristics facilitate efficient and stable ion transport across the full cell.

In all-solid-state batteries, where charge transport relies entirely on solid-solid interfaces, dynamically resolving interfacial resistance is essential. We applied distribution of relaxation times (DRT) analysis to in situ electrochemical impedance spectra collected over the first three cycles of an NNFMO | NZPOC* | NPS | Na_2Sn full cell. The derived DRT spectra (Figures 5g and S46–S51) resolve six distinct peaks (P1-P6) [37, 38], each

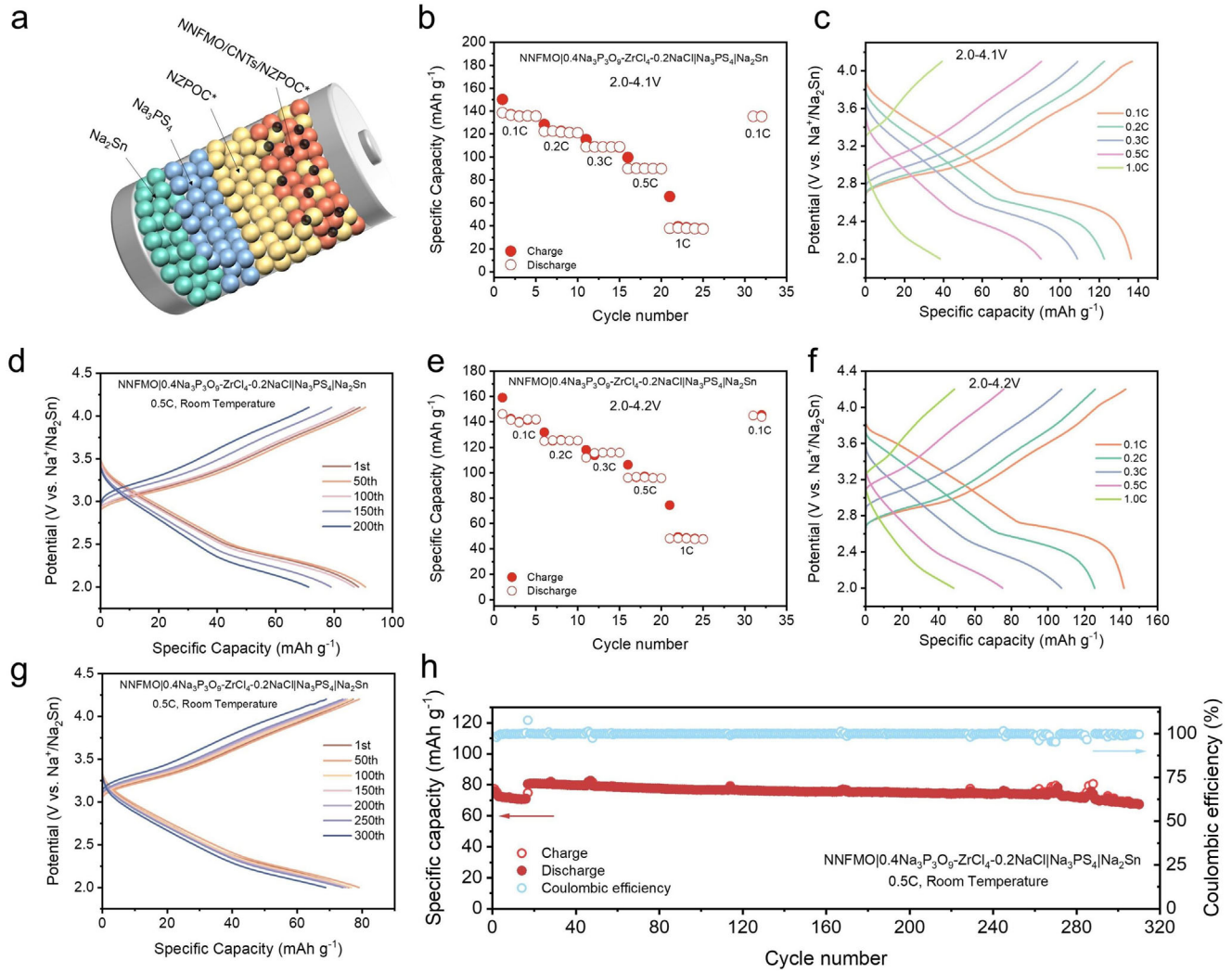

FIGURE 4 | (a) Schematic diagram of sodium-ion all-solid-state battery (ASSNIB). (b, c) Rate performance and charge–discharge curves extracted from rate performance measurements of the NNFMO ASSNIBs at room temperature (RT, 25°C) with NZPOC*, in the voltage range of 2.0–4.1 V versus Na^+ / Na_2Sn. (d) Charge–discharge profiles of the selected cycles of ASSNIB with NNFMO cathode at 0.5C (2.0–4.1 V versus Na^+ / Na_2Sn). (e, f) Rate performance and charge–discharge curves extracted from rate performance measurements of the NNFMO ASSNIBs at room temperature (RT, 25°C) with NZPOC*, in the voltage range of 2.0–4.2 V versus Na^+ / Na_2Sn. (g, h) Galvanostatic voltage profiles (g) and specific capacities (h) of ASSNIBs as a function of cycle number, running at 0.5C and room temperature (RT, 25°C), in the voltage range of 2.0–4.2 V versus Na^+ / Na_2Sn.

corresponding to a specific interfacial or bulk process: P1 arises from intergrain contact within the electrolyte bulk; P2 originates from contact between electrode particles and the current collector; P3 is attributed to Na^+ migration across either the cathode/electrolyte or the anode (NPS/Na_2Sn alloy) interface; P4 and P5 are associated with charge transfer at the anode and cathode interfaces, respectively [39, 40]; and P6, characterized by the largest time constant (frequency < 0.1 Hz), corresponds to solid-state diffusion within the electrode material. The highly state-dependent evolution of the P6 peak (Figure 5h) reveals kinetically slowed sodiation toward the end of discharge [41]. This behavior results from increasingly hindered solid-state diffusion within the cathode as Na^+ site occupancy rises, which elevates the energy barrier for further sodium insertion at high states of charge.

6 | Conclusion

In conclusion, we have pioneered the use of the cyclic trimetaphosphate anion ($P_3O_9^{3-}$) as a superior network-forming unit to construct a new family of amorphous oxyhalide SSEs via a facile mechanochemical route. This molecular design overcomes the classical "trilemma" in SSE development by integrating three key features: (1) a robust 3D amorphous framework formed through multidentate coordination of $P_3O_9^{3-}$ with high-valent metal chlorides, (2) a synergistic ion transport mechanism, wherein the stable $P_3O_9^{3-}$-bridged network provides continuous Na^+ migration channels while dynamically mobile Cl^- anions assist hopping by mitigating steric and electrostatic barriers, and (3) an inherent thermodynamic driving force that enables mild synthesis and structural flexibility. The optimized

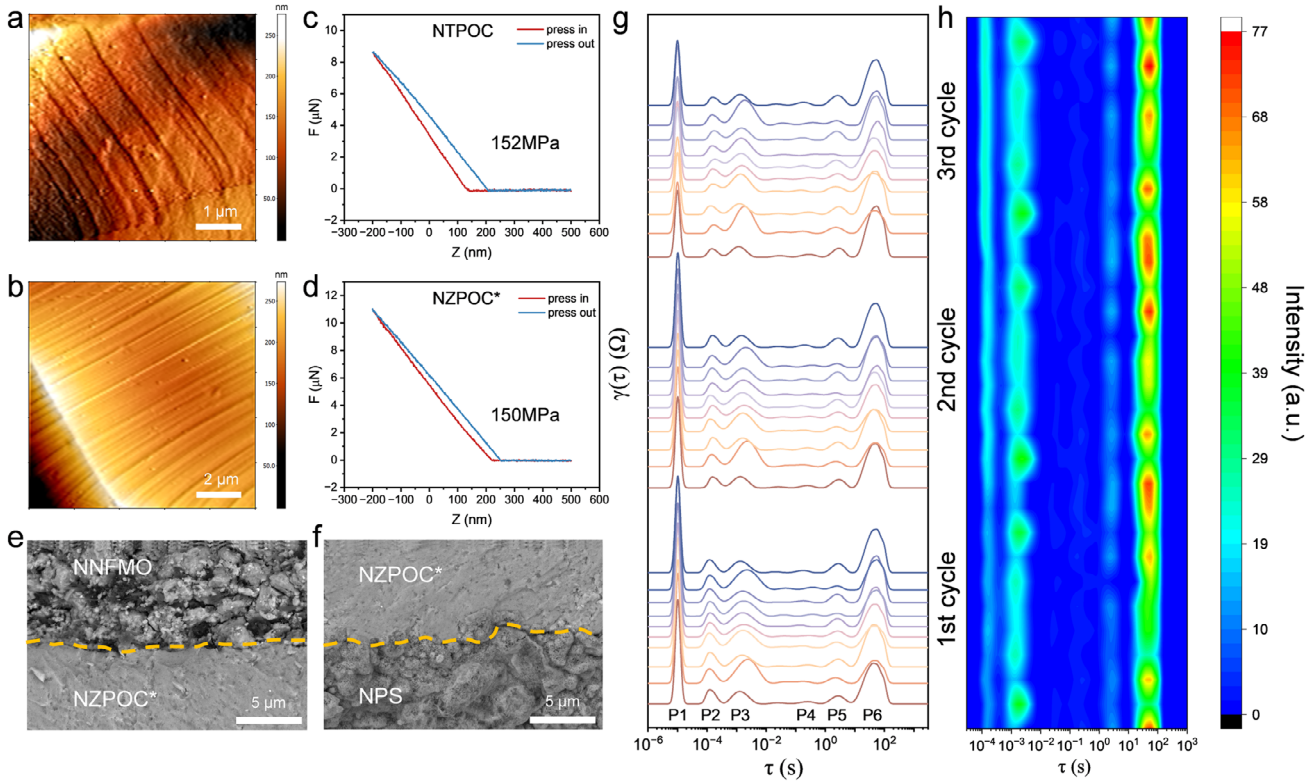

FIGURE 5 | (a–d) Single-molecule force spectroscopy curves acquired by atomic force microscopy (AFM) for NTPOC (a, c) and NZPOC*(b, d) SSEs. (e, f) Scanning electron microscopy images of the interphase between the cathode composite and NZPOC* electrolyte layer (e) and the interphase between the NPS and NZPOC* electrolyte layer (f). (g) Distribution of relaxation times spectra calculated from EIS measurements. The τ represents relaxation time, and $\gamma(\tau)$ stands for distribution function of relaxation times. (h) Two-dimensional intensity color map of the charge-dependent and discharge-dependent distribution of relaxation times curves abstracted from (f).

electrolyte exhibits a high room-temperature ionic conductivity of 0.80 mS·cm^{-1}, an ultrawide electrochemical window of 1.4–4.2 V, and excellent mechanical compliance (Young's modulus ~0.15 GPa). When configured in a full cell with a high-voltage $NaNi_{0.33}Fe_{0.33}Mn_{0.33}O_2$ cathode, the electrolyte enables stable cycling at 4.2 V, retaining 92% capacity after 300 cycles at 0.5C. Overall, this work establishes a new paradigm for SSE design— "macrocyclic polyanion network + thermodynamic-enabled synthesis + dynamic anion-assisted transport" —that simultaneously addresses ionic conductivity, electrochemical stability, and interfacial compatibility. It not only opens a promising avenue for practical high-voltage ASSNIBs but also provides a generalizable strategy for designing next-generation solid electrolytes beyond sodium systems.

Author Contributions

Siyuan Zhang: investigation, methodology, validation, writing – original draft, formal analysis, conceptualization, funding acquisition, writing – review and editing. **Jiacong Li:** investigation, funding acquisition, writing – review and editing, writing – original draft, methodology, validation, project administration, conceptualization. **Yuge Cao:** conceptualization, investigation, funding acquisition, writing – review and editing, methodology. **Yifeng Zhao:** investigation, methodology, validation. **Zhongxing Xu:** investigation. **Zhuoran Lv:** investigation. **Long Yang:** software. **Chaohong Guan:** software. **Zhangliu Tian:** investigation. **Wujie Dong:** conceptualization, investigation, funding acquisition, writing – original draft, methodology, validation, visualization, writing – review and editing. **Haijie Chen:** investigation. **Fuqiang Huang:** conceptualization, investigation, funding acquisition, writing – original draft, methodology, validation, visualization, writing – review and editing.

Acknowledgments

This work was supported by the National Key R&D Program of China (Grant Number. 2025YFF0516300), then Joint Fund of the National Natural Science Foundation of China (Grant Number. 22561160126, 22471283, 52402287), the National Natural Science Foundation of China (Grant Number. 52302193), and the Fundamental Research Funds for the Central Universities, Science and Technology Commission of Shanghai Municipality (23DZ1200800), and Science and Technology Cooperation Program of Shanghai Jiao Tong in Inner Mongolia Autonomous Region——Action Plan of Shanghai Jiao Tong University for Revitalizing Inner Mongolia through Science and Technology. The authors would also like to the Shanghai Synchrotron Radiation Facility of BL14W1 (https://cstr.cn/31124.02.SSRF.BL14W1) and BL11B (https://cstr.cn/31124.02.SSRF.BL11B) for the assistance on XAFS measurements. The authors also thank the Shanghai Synchrotron Radiation Facility of BL12SW (http://cstr.cn/31124.02.SSRF.BL12SW) for the assistance on PDF measurements.

Conflicts of Interest

The authors declare no conflict of interest.

Data Availability Statement

The data that support the findings of this study are available from the corresponding author upon reasonable request.

References

1. Y. Li, X. Tang, Q. Li, et al., "Halide Solid-State Electrolytes for All-Solid-State Sodium Batteries: Progress and Perspectives," *ACS Energy Letters* 10 (2025): 5520–5541, https://doi.org/10.1021/acsenergylett.5c02748.

2. Y. Nikodimos, W. N. Su, and B. J. Hwang, "Halide Solid-State Electrolytes: Stability and Application for High Voltage All-Solid-State Li Batteries," *Advanced Energy Materials* 13 (2022):2202854.

3. K. Tuo, C. Sun, and S. Liu, "Recent Progress in and Perspectives on Emerging Halide Superionic Conductors for All-Solid-State Batteries," *Electrochemical Energy Reviews* 6 (2023): 17, https://doi.org/10.1007/s41918-023-00179-5.

4. C. Yang, S. Xin, L. Mai, and Y. You, "Materials Design for High-Safety Sodium-Ion Battery," *Advanced Energy Materials* 11 (2020):2000974.

5. M. Wu, H. Liu, X. Qi, et al., "Structure Designing, Interface Engineering, and Application Prospects for Sodium-Ion Inorganic Solid Electrolytes," *InfoMat* 6 (2024): e12606, https://doi.org/10.1002/inf2.12606.

6. M. Akbar, I. Moeez, A. H. Umar Bhatti, et al., "Antimony-doped NASICON-type Solid Electrolyte With Homogeneous Sodium-ion Flux for High-Temperature Solid-State Sodium Batteries," *Chemical Engineering Journal* 517 (2025): 164300, https://doi.org/10.1016/j.cej.2025.164300.

7. K. Singh, A. Chakraborty, R. Thirupathi, and S. Omar, "Recent Advances in NASICON-Type Oxide Electrolytes for Solid-State Sodium-Ion Rechargeable Batteries," *Ionics* 28 (2022): 5289–5319, https://doi.org/10.1007/s11581-022-04765-3.

8. A. Hayashi, N. Masuzawa, S. Yubuchi, et al., "A Sodium-Ion Sulfide Solid Electrolyte With Unprecedented Conductivity at Room Temperature," *Nature Communications* 10 (2019): 5266.

9. A. Sundar, T. Kim, F. Lagunas, et al., "Computationally-Guided Development of Sulfide Solid Electrolyte Powder Coatings for Enhanced Stability and Performance of Solid-State Batteries," *Advanced Science* 12 (2025): e13191, https://doi.org/10.1002/advs.202513191.

10. R. Schlem, A. Banik, S. Ohno, E. Suard, and W. G. Zeier, "Insights Into the Lithium Sub-Structure of Superionic Conductors Li_3YCl_6 and Li_3YBr_6," *Chemistry of Materials* 33 (2021): 327–337, https://doi.org/10.1021/acs.chemmater.0c04352.

11. H. Tian, J. Li, Y. Cai, X. Yao, and Z. Su, "Dendrite-Free, Interfacially Compatible Na_2ZrCl_6 Composite Halide Solid-State Electrolyte for Solid-State Sodium-Ion Batteries," *Journal of Materials Chemistry A* 13 (2025): 15178–15188, https://doi.org/10.1039/D4TA07957D.

12. G. Wang, S. Zhang, H. Wu, et al., "Oxychloride Polyanion Clustered Solid-State Electrolytes via Hydrate-Assisted Synthesis for all-Solid-State Batteries," *Advanced Materials* 37 (2024): 2410402.

13. X. Wang, S. Zhang, J. Yue, et al., "A New Class of Carbonate–Oxychloride Solid Electrolytes for High-performance Sodium-Ion All-Solid-State Batteries," *Energy & Environmental Science* 18 (2025): 9927–9938, https://doi.org/10.1039/D5EE03490F.

14. E. Milan and M. Pasta, "The Role of Grain Boundaries in Solid-State Li-metal Batteries," *Materials Futures* 2 (2023): 013501, https://doi.org/10.1088/2752-5724/aca703.

15. H. Kwak, J.-S. Kim, D. Han, et al., "Boosting the Interfacial Superionic Conduction of Halide Solid Electrolytes for All-Solid-State Batteries," *Nature Communications* 14 (2023): 2459, https://doi.org/10.1038/s41467-023-38037-z.

16. J. Yue, S. Zhang, X. Wang, et al., "Universal Superionic Conduction via Solid Dissociation of Salts in van der Waals Materials," *Nature Energy* 10 (2025): 1237–1250, https://doi.org/10.1038/s41560-025-01853-2.

17. J. Qu, H. Wu, X. Wang, et al., "Advances in Non/Low-crystalline Solid-State Electrolytes Enabled by Halide-Based Electrolytes," *Joule* 10 (2026): 102260, https://doi.org/10.1016/j.joule.2025.102260.

18. J. Fu, S. Wang, D. Wu, et al., "Halide Heterogeneous Structure Boosting Ionic Diffusion and High-Voltage Stability of Sodium Superionic Conductors," *Advanced Materials* 36 (2024): e2308012, https://doi.org/10.1002/adma.202308012.

19. Y. Song, S. Xue, Z. Xu, et al., "1D $ZrCl_4$ Matrices for Enhanced Ion Transport in Glassy Chloride Electrolytes," *Advanced Energy Materials* 15 (2025): 2500913.

20. B. Hong, L. Gao, P. Nan, et al., "Novel Amorphous Nitride-Halide Solid Electrolytes With Enhanced Performance for all-Solid-State Batteries," *Angewandte Chemie International Edition* 64 (2024): e202415847.

21. J. A. Newnham, J. Kondek, J. Hartel, et al., "Correlation Between the Coherence Length and Ionic Conductivity in $LiNbOCl_4$ via the Anion Stoichiometry," *Chemistry of Materials* 37 (2025): 4130–4144, https://doi.org/10.1021/acs.chemmater.5c00627.

22. E. A. Wu, S. Banerjee, H. Tang, et al., "A Stable Cathode-Solid Electrolyte Composite for High-Voltage, Long-Cycle-Life Solid-State Sodium-Ion Batteries," *Nature Communications* 12 (2021): 1256, https://doi.org/10.1038/s41467-021-21488-7.

23. M. Wu, X. Liu, H. Liu, et al., "Fluorinated Amorphous Halides With Improved Ionic Conduction and Stability for all-solid-state Sodium-ion Batteries," *Nature Communications* 16 (2025): 2808, https://doi.org/10.1038/s41467-025-58113-w.

24. H. Kwak, J. Lyoo, J. Park, et al., "Na_2ZrCl_6 enabling Highly Stable 3 V All-Solid-State Na-Ion Batteries," *Energy Storage Materials* 37 (2021): 47–54, https://doi.org/10.1016/j.ensm.2021.01.026.

25. L. Hu, H. Li, F. Chen, Y. Liu, J. Wang, and C. Ma, "Overcoming the Na-Ion Conductivity Bottleneck for the Cost-Competitive Chloride Solid Electrolytes," *Journal of Energy Chemistry* 95 (2024): 1–8, https://doi.org/10.1016/j.jechem.2024.03.023.

26. S. Chaoudhary, A. Aumen, E. C. Dickey, and A. Klein, "Direct Determination of the Charge Transition Level of Dopants in Oxides by X-ray Photoelectron Spectroscopy," *Physical Review Materials* 9 (2025): 075002, https://doi.org/10.1103/mg9m-hk3n.

27. H. W. Nesbitt, G. M. Bancroft, G. S. Henderson, et al., "Bridging, Non-Bridging and Free (O^{2-}) Oxygen in Na_2O-SiO_2 Glasses: An X-ray Photoelectron Spectroscopic (XPS) and Nuclear Magnetic Resonance (NMR) Study," *Journal of Non-Crystalline Solids* 357 (2011): 170–180, https://doi.org/10.1016/j.jnoncrysol.2010.09.031.

28. R. Christensen, G. Olson, and S. W. Martin, "Ionic Conductivity of Mixed Glass Former $0.35Na_2O + 0.65[x B_2O_3 + (1 - x)P_2O_5]$ Glasses," *Journal of Physical Chemistry B* 117 (2013): 16577–16586, https://doi.org/10.1021/jp409497z.

29. W. Li, J. Liang, M. Li, et al., "Unraveling the Origin of Moisture Stability of Halide Solid-State Electrolytes by in Situ and Operando Synchrotron X-ray Analytical Techniques," *Chemistry of Materials* 32 (2020): 7019–7027, https://doi.org/10.1021/acs.chemmater.0c02419.

30. Z. Xia, H. Zhang, K. Shen, Y. Qu, and Z. Jiang, "Wavelet Analysis of Extended X-ray Absorption Fine Structure Data: Theory, Application," *Physica B: Condensed Matter* 542 (2018): 12–19, https://doi.org/10.1016/j.physb.2018.04.039.

31. M. Muñoz, P. Argoul, and F. Farges, "Continuous Cauchy Wavelet Transform Analyses of EXAFS Spectra: A Qualitative Approach," *The American Mineralogist* 88 (2003): 694–700, https://doi.org/10.2138/am-2003-0423.

32. M. Muñoz, P. Argoul, and F. Farges, "Continuous Cauchy Wavelet Transform Analyses of EXAFS Spectra: A Qualitative Approach," 88 (2003): 694–700.

33. N. Bloembergen, E. M. Purcell, and R. V. Pound, "Relaxation Effects in Nuclear Magnetic Resonance Absorption," *Physical Review* 73 (1948): 679–712, https://doi.org/10.1103/PhysRev.73.679.

34. X. Lin, Y. Zhao, C. Wang, et al., "A Dual Anion Chemistry-Based Superionic Glass Enabling Long-Cycling All-Solid-State Sodium-Ion Batteries," *Angewandte Chemie* 63 (2024): e202314181, https://doi.org/10.1002/anie.202314181.

35. Y. Hu, J. Fu, J. Xu, et al., "Superionic Amorphous $NaTaCl_6$ Halide Electrolyte for Highly Reversible All-Solid-State Na-Ion Batteries," *Matter* 7 (2024): 1018–1034, https://doi.org/10.1016/j.matt.2023.12.017.

36. G. Wei, L. Binci, and G. Ceder, "Microscopic Mechanisms of Superionic Na-Ion Conductivity in Crystalline and Amorphous $NaMOCl_4$ (M = Nb, Ta) Solid Electrolytes," *ACS Energy Letters* 11 (2026): 1861–1870, https://pubs.acs.org/doi/10.1021/acsenergylett.5c03511.

37. X. Chen, L. Li, M. Liu, T. Huang, and A. Yu, "Detection of Lithium Plating in Lithium-Ion Batteries by Distribution of Relaxation Times," *Journal of Power Sources* 496 (2021): 229867, https://doi.org/10.1016/j.jpowsour.2021.229867.

38. X. Li, J. Liang, J. T. Kim, et al., "Highly Stable Halide-Electrolyte-Based All-Solid-State Li–Se Batteries," *Advanced Materials* 34 (2022): 2200856, https://doi.org/10.1002/adma.202200856.

39. P. Gargh, A. Sarkar, Y. H. Lui, et al., "Correlating Capacity Fade With Film Resistance Loss in Fast Charging of Lithium-Ion Battery," *Journal of Power Sources* 485 (2021): 229360, https://doi.org/10.1016/j.jpowsour.2020.229360.

40. J. Illig, J. P. Schmidt, M. Weiss, A. Weber, and E. Ivers-Tiffée, "Understanding the Impedance Spectrum of 18650 $LiFePO_4$-cells," *Journal of Power Sources* 239 (2013): 670–679, https://doi.org/10.1016/j.jpowsour.2012.12.020.

41. W. Zhang, D. A. Weber, H. Weigand, et al., "Interfacial Processes and Influence of Composite Cathode Microstructure Controlling the Performance of all-Solid-State Lithium Batteries," *ACS Applied Materials & Interfaces* 9 (2017): 17835–17845, https://doi.org/10.1021/acsami.7b01137.

Supporting Information

Additional supporting information can be found online in the Supporting Information section.

Supporting File: anie73283-sup-0001-SuppMat.docx.